Received: 15 February 2020 | Revised: 5 March 2020 | Accepted: 5 March 2020

DOI: 10.1002/eom2.12021

RESEARCH ARTICLE

EcoMat FUNCTIONAL MATERIALS FOR GREEN ENERGY AND ENVIRONMENT WILEY

Boosting oxygen evolution reaction by activation of lattice-oxygen sites in layered Ruddlesden-Popper oxide

Yinlong Zhu[1] | Hassan A. Tahini[2] | Zhiwei Hu[3] | Yichun Yin[1] | Qian Lin[1] | Hainan Sun[4] | Yijun Zhong[5] | Yubo Chen[6] | Feifei Zhang[1] | Hong-Ji Lin[7] | Chien-Te Chen[7] | Wei Zhou[4] | Xiwang Zhang[1] | Sean C. Smith[2] | Zongping Shao[4,5] | Huanting Wang[1]

[1]Department of Chemical Engineering, Monash University, Clayton, Victoria, Australia

[2]Integrated Materials Design Laboratory, Department of Applied Mathematics, Research School of Physics and Engineering, Australian National University, Canberra, Australian Capital Territory, Australia

[3]Max Planck Institute for Chemical Physics of Solids, Dresden, Germany

[4]State Key Laboratory of Materials-Oriented Chemical Engineering, College of Chemical Engineering, Nanjing Tech University, Nanjing, China

[5]Department of Chemical Engineering, Curtin University, Perth, Western Australia, Australia

[6]School of Material Science and Engineering, Nanyang Technological University, Singapore

[7]National Synchrotron Radiation Research Center, Hsinchu, Taiwan

Correspondence
Yinlong Zhu and Huanting Wang, Department of Chemical Engineering, Monash University, Clayton 3800, Victoria, Australia.
Email: yinlong.zhu@monash.edu (Y. Z.) and huanting.wang@monash.edu (H. W.)

Wei Zhou, State Key Laboratory of Materials-Oriented Chemical Engineering, College of Chemical Engineering, Nanjing Tech University, Nanjing 211816, China.
Email: zhouwei1982@njtech.edu.cn

Funding information
Government of Western Australia; Australian National Computational; Australian Research Council, Grant/Award Number: DE190100005

Abstract

Emerging anionic redox chemistry presents new opportunities for enhancing oxygen evolution reaction (OER) activity considering that lattice-oxygen oxidation mechanism (LOM) could bypass thermodynamic limitation of conventional metal-ion participation mechanism. Thus, finding an effective method to activate lattice-oxygen in metal oxides is highly attractive for designing efficient OER electrocatalysts. Here, we discover that the lattice-oxygen sites in Ruddlesden-Popper (RP) crystal structure can be activated, leading to a new class of extremely active OER catalyst. As a proof-of-concept, the RP $Sr_3(Co_{0.8}Fe_{0.1}Nb_{0.1})_2O_{7-\delta}$ (RP-SCFN) oxide exhibits outstanding OER activity (eg, 334 mV at 10 mA cm^{-2} in 0.1 M KOH), which is significantly higher than that of the simple $SrCo_{0.8}Fe_{0.1}Nb_{0.1}O_{3-\delta}$ perovskite and benchmark RuO_2. Combined density functional theory and X-ray absorption spectroscopy studies demonstrate that RP-SCFN follows the LOM under OER condition, and the activated lattice oxygen sites triggered by high covalency of metal-oxygen bonds are the origin of the high catalytic activity.

KEYWORDS

anion activation, lattice-oxygen sites, oxygen evolution reaction, Ruddlesden-Popper oxide, structure engineering

1 | INTRODUCTION

Research into the oxygen evolution reaction (OER) has been of particular interest, as it plays a critical role in multiple electrochemical energy conversion and storage technologies such as regenerative fuel cells, rechargeable metal-air batteries, water splitting, and CO_2 reduction.[1-3] Nevertheless, the sluggish kinetics of OER limits the overall efficiency of these electrochemical systems due to complex four-electron oxidation process, hence calling for efficient electrocatalysts to accelerate.[3] Currently, the benchmark OER electrocatalysts are precious metal-based oxides (ie, RuO_2 and IrO_2); however, the problems of high cost and low abundance of these metals make them unsuitable for commercial scale application. Great efforts have been thus devoted to the search for efficient alternative OER catalysts composed of low-cost and earth-abundant elements.

As an important family of functional materials, perovskite-type metal oxides with a general formula of ABO_3 (A = alkaline-earth or rare-earth metals; B = transition metals) have emerged as promising OER electrocataysts during the past few decades.[4-7] Traditionally, the OER catalytic activity of perovskite oxides is dominated by the cationic redox centers (ie, the B-site transition metal cations are regarded as active sites). In view of this, some descriptors related to the electronic structure of B-site transition metals, such as e_g orbital occupancy,[8] d electron number,[9] and magnetism,[10] have been well correlated with the OER activity. As such, some well-known perovskites with high intrinsic OER activity have been developed, for example, $Ba_{0.5}Sr_{0.5}Co_{0.8}Fe_{0.2}O_{3-\delta}$[8] and $SrCo_{0.7}Fe_{0.2}Nb_{0.1}O_{3-\delta}$ (SCFN).[11] However, this conventional mechanism concerning cation redox was recently challenged by few experimental and theoretical studies.[12-17] A new OER mechanism involving lattice-oxygen participation for perovskite oxides was proposed and increased metal-oxygen covalency was found to be critical to promote the OER kinetics.[14-17] By advanced *in-situ* ^{18}O isotope labeling mass spectrometry, Grimaud et al gave a direct experimental evidence that the generated O_2 during OER on some highly covalent perovskite oxides comes from lattice oxygen.[17] These findings highlight the significance of surface lattice oxygen in OER catalysis and open an exciting opportunity for designing highly active oxide-based catalysts. However, up to date, catalysts via lattice-oxygen oxidation mechanism (LOM) for OER are still very limited. Therefore, it is highly desirable but challenging to develop highly active electrocatalysts with lattice-oxygen active sites.

Apart from the simple perovskite oxides, complex metal oxides with special crystal structure have been widely used in various fields by virtue of their fascinating physical-chemical properties.[18-22] Diverse crystal structures of complex oxides can trigger some novel geometrical, electronic, and conductive properties, consequently promoting the electrocatalytic performance. Among various complex oxides, Ruddlesden-Popper (RP) type oxides (formula of $A_{n+1}B_nO_{3n+1}$ or equivalently [AO] $(ABO_{3\pm\delta})_n$), wherein n ABO_3 perovskite layers are sandwiched between two AO rock-salt layers, have received considerable attention due to their chemical flexibility, layered structure, wide element accommodation, and labile lattice oxygen.[23-26] The RP phase possesses preferential formation of oxygen vacancies at the apical O-site pointing toward the rock-salt layers,[26,27] which provides high possibility of lattice oxygen-participated OER in RP structure.[24]

Herein, we report that the lattice-oxygen sites of RP structure can be effectively activated by designing a suitable composition to achieve the exceptionally high OER activity. In particular, RP $Sr_3(Co_{0.8}Fe_{0.1}Nb_{0.1})_2O_{7-\delta}$ (RP-SCFN) is synthesized as an RP catalyst to demonstrate this new strategy. When tested on glass carbon electrode in 0.1 M KOH solution, the RP-SCFN material achieves the 10 mA cm^{-2} at an extremely low overpotential of 334 mV, outperforming the benchmark RuO_2 catalyst and nearly any metal oxides reported to date. Moreover, the RP-SCFN exhibits much higher mass activity (MA) and specific activity (SA) than the simple $SrCo_{0.8}Fe_{0.1}Nb_{0.1}O_{3-\delta}$ perovskite (P-SCFN). First-principle calculations reveal that the OER on the RP-SCFN proceeds via the LOM pathway with a low theoretical thermodynamic overpotential of 0.22 V, which originates from the strong metal-oxygen covalency as confirmed by advanced soft X-ray absorption spectroscopy (sXAS) technique. This work suggests the potential of RP oxides as efficient and economic OER catalysts involving lattice oxygen sites.

2 | RESULT AND DISCUSSION

2.1 | Crystal structure characterization

In the idea cubic-symmetry ABO_3 perovskite structure, larger A-site cations (eg, Sr) are 12-fold oxygen coordination and smaller B-site cations (eg, Co/Fe/Nb) are sixfold oxygen coordinated (Figure 1A). RP structure with the chemical formula of $A_3B_2O_7$ is a layered structure, which consist of alternative perovskite ABO_3 layer and rock-salt AO layer along the c-direction (Figure 1B). $SrCo_{0.8}Fe_{0.1}Nb_{0.1}O_{3-\delta}$ perovskite (denoted as P-SCFN) and RP $Sr_3(Co_{0.8}Fe_{0.1}Nb_{0.1})_2O_{7-\delta}$ oxide (denoted as RP-SCFN) were successfully synthesized using a facile and scalable sol-gel method, and their crystal structures were initially verified by X-ray diffraction (XRD) (Figure 1C). Rietveld refinement of the XRD pattern demonstrates that the RP-SCFN adopts a pure tetragonal structure with a space group of *I*4/mmm and unit cell parameters of $a = b = 3.8531(2)$ Å, $c = 20.144(1)$ Å (Figure 1D).

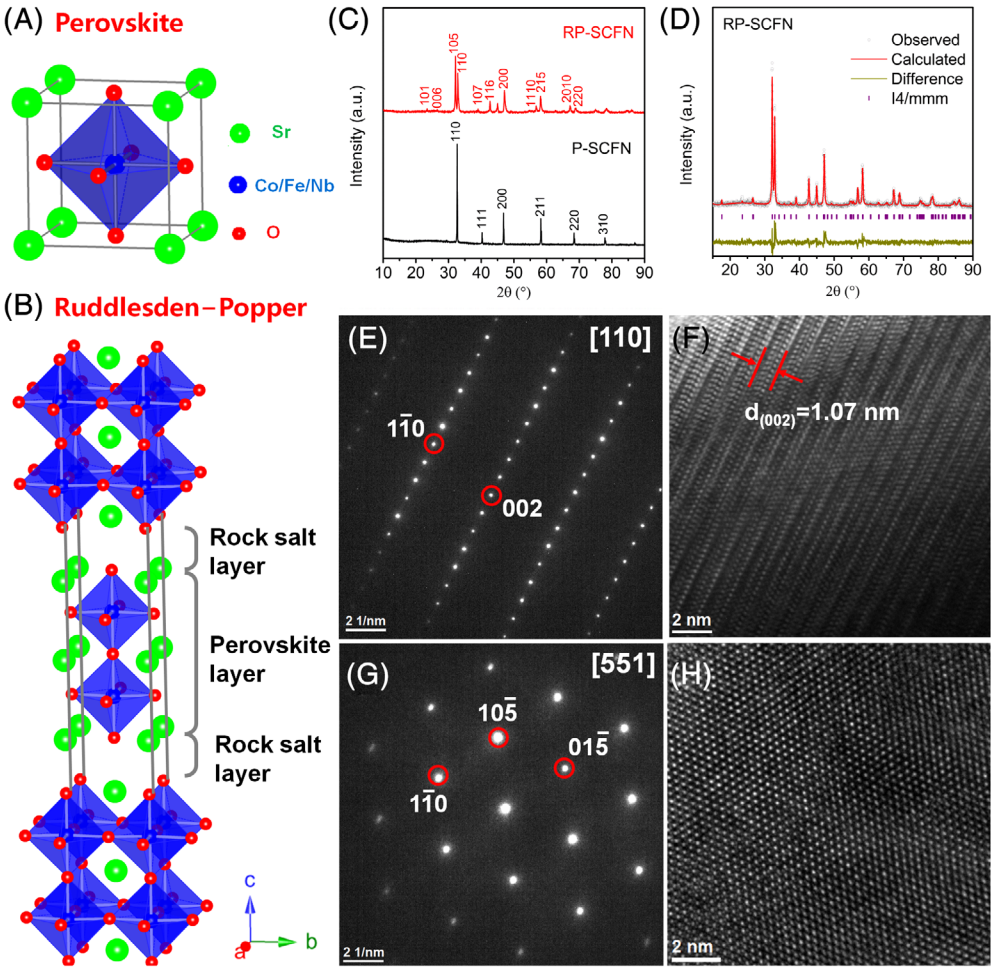

FIGURE 1 Schematic presentation of, A, perovskite structure and, B, layered Ruddlesden-Popper structure. C, XRD patterns of RP-SCFN and P-SCFN. D, Refined XRD profile of the RP-SCFN. E and G, SAED patterns and the corresponding HRTEM images, F and H, along the [110] and [551] zone axes for RP-SCFN. HRTEM, high-resolution transmission electron microscopy; P-SCFN, $SrCo_{0.8}Fe_{0.1}Nb_{0.1}O_{3-\delta}$ perovskite; RP-SCFN, Ruddlesden-Popper $Sr_3(Co_{0.8}Fe_{0.1}Nb_{0.1})_2O_{7-\delta}$; SAED, selected-area electron-diffraction; XRD, X-ray diffraction

The crystal structure of RP-SCFN was further confirmed by two selected-area electron-diffraction patterns along the [110] and [551] zone axes (Figure 1E,G) and the corresponding high-resolution transmission electron microscopy images (Figure 1F,H). Scanning electron microscopy images show that the P-SCFN and RP-SCFN powders are both composed of micron-sized particles (but slightly smaller size is observed for RP-SCFN) (Figure S1), suggesting the bulk nature of the as-prepared powders. In addition, in order to investigate the effect of composed elements (eg, Nb and Fe) on the crystal structure of RP-SCFN, we also attempted to synthesize $Sr_3Co_2O_{7-\delta}$ (RP-SC), $Sr_3(Co_{0.9}Fe_{0.1})_2O_{7-\delta}$ (RP-SCF), and $Sr_3(Co_{0.9-x}Fe_xNb_{0.1})_2O_{7-\delta}$ with different Fe substitutions (x = 0, 0.2, 0.3, 0.4, and 1) under the same conditions. In Figure S2, pure RP phase was observed in $Sr_3(Co_{0.9-x}Fe_xNb_{0.1})_2O_{7-\delta}$ while Nb-free RP-SC and RP-SCF could not form pure RP structure, implying the key role of Nb^{5+} on stabilizing the RP structure as also reported elsewhere.[28,29]

2.2 | Electrocatalytic OER measurement

The OER electrocatalytic activity of RP-SCFN and P-SCFN catalysts was assessed by a typical thin-film rotating disk electrode technique.[8,30,31] Similar measurements were also conducted on the benchmark RuO_2 catalyst for comparison (Figure S3). Unless indicated otherwise, all data in our work were corrected to reversible hydrogen electrode (Figure S4) and *iR*-corrected for compensating the electrolyte resistance. Figure 2A shows the capacitance- and Ohmic resistance-corrected polarization curves acquired from cycle voltammetry (Figure S5) of RP-SCFN, P-SCFN, and RuO_2 catalysts on glassy carbon (GC) in 0.1 M KOH solution. The electrode activity of RP-SCFN distinctly exceeds that of P-SCFN and benchmark RuO_2, as indicated by the smaller onset potential of ~1.45 V and higher catalytic current. The overpotential (η) required to deliver a 10 mA cm^{-2} is a metric associated with solar fuel synthesis and widely used as a parameter for activity comparison.[32,33] Strikingly, the RP-SCFN displays an extremely small η of only 334 mV, much lower than that of P-SCFN and RuO_2. To evaluate the activity more comprehensively, the MA normalized to the catalyst mass loading and SA normalized to real oxide surface area (as estimated from BET measurements, Table S1 and Figure S6) were calculated. As seen from Figure 2B, the RP-SCFN achieves an MA of 80.7 A g^{-1} at η = 0.35 V, which is ~ 81 and ~6 times higher than that

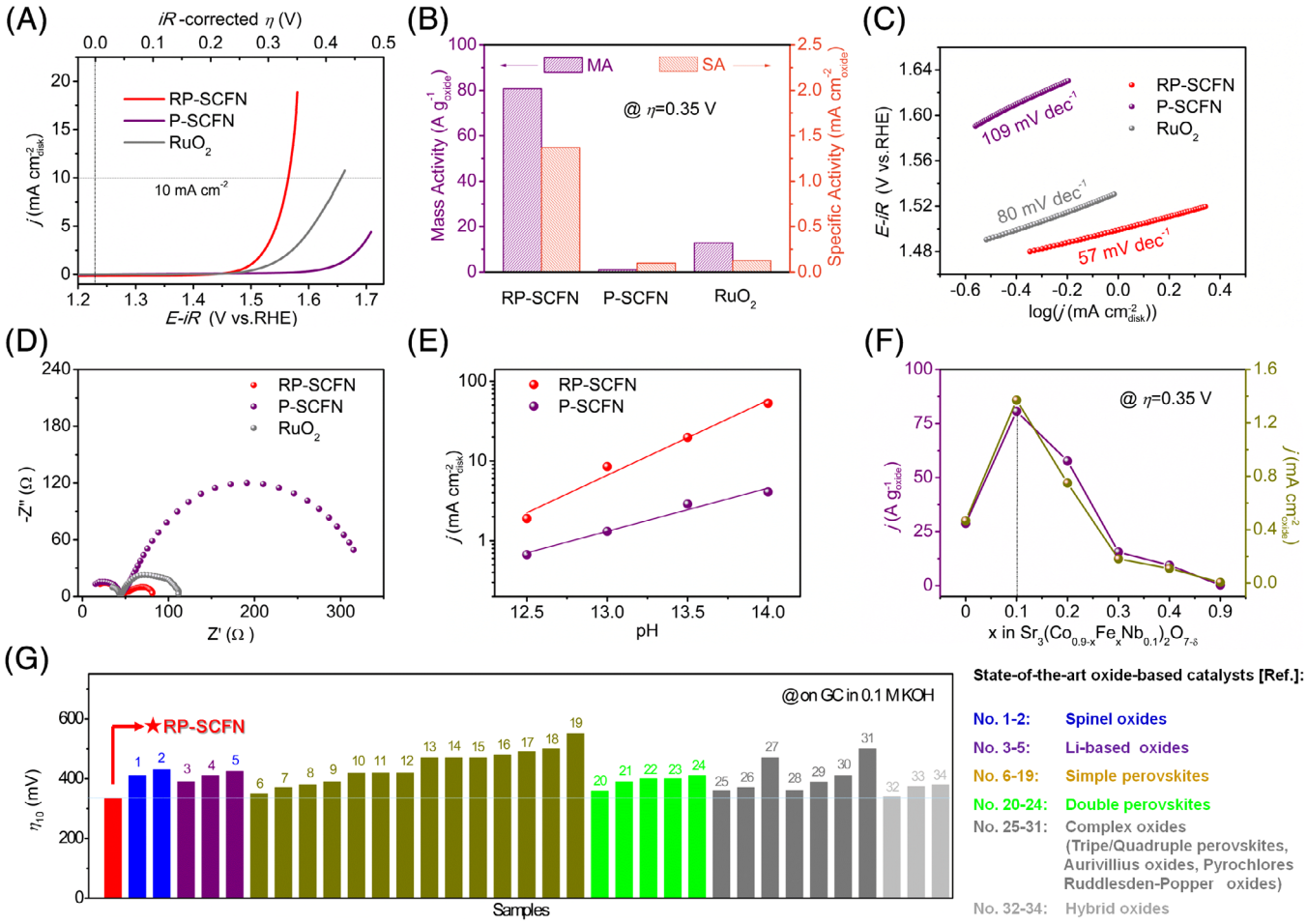

FIGURE 2 A, Capacitance- and Ohmic resistance-corrected polarization curves of RP-SCFN, P-SCFN, and RuO_2 catalysts in O_2-saturated 0.1 M KOH solution. B, Mass activities and specific activities of RP-SCFN, P-SCFN, and RuO_2 catalysts at $\eta = 0.35$ V. C, Tafel plots derived from the data shown in A. D, Nyquist plots of RP-SCFN, P-SCFN, and RuO_2 catalysts recorded at 0.7 V vs Ag/AgCl under the influence of an AC voltage of 10 mV. E, Current densities of RP-SCFN and P-SCFN at 0.7 V vs Ag/AgCl as a function of the pH value. F, Mass activities and specific activities of $Sr_3(Co_{0.9-x}Fe_xNb_{0.1})_2O_{7-\delta}$ (x = 0, 0.1, 0.2, 0.3, 0.4, 1) catalysts at $\eta = 0.35$ V. G, Comparison of η_{10} between RP-SCFN and reported state-of-the-art oxide-based catalysts supported on glass carbon electrode in 0.1 M KOH. P-SCFN, $SrCo_{0.8}Fe_{0.1}Nb_{0.1}O_{3-\delta}$ perovskite; RP-SCFN, Ruddlesden-Popper $Sr_3(Co_{0.8}Fe_{0.1}Nb_{0.1})_2O_{7-\delta}$

of P-SCFN (1.0 A g^{-1}) and RuO_2 (12.9 A g^{-1}). Besides the MA, the SA of RP-SCFN is ~14 times higher than that of P-SCFN, suggesting the considerable intrinsic activity enhancement by structure engineering. To examine the kinetics, Tafel plots were constructed in Figure 2C. The Tafel slope for RP-SCFN (57 mV dec^{-1}) is smaller than that for hex-BSC (109 mV dec^{-1}) and RuO_2 (80 mV dec^{-1}) catalysts, implying more rapid OER rates. Electrochemical impedance spectroscopy tests were further performed to examine the kinetics during OER process. Smaller charge transfer resistance (R_{ct}) of RP-SCFN was observed than P-SCFN and RuO_2 (Figure 2D), corresponding to better charge transfer abilities for OER catalysis. As a whole, all above electrochemical analyses (including low overpotential, low Tafel slope, high MA, and SA) highlight the outstanding catalytic activity of RP-SCFN for OER.

It was reported that some highly active oxides enabling lattice oxygen-oxidation typically displays pH-dependent OER activity, involving nonconcerted proton-electron transfers in the OER mechanism.[17,34] The OER activity of RP-SCFN was then examined in KOH solutions at different pH values (Figure S7). As a result, the RP-SCFN catalyst exhibits much stronger pH-dependent OER activity than P-SCFN (Figure 2E), which implies that the OER proceeds on RP-SCFN via the participation of lattice oxygen. In addition, what is noteworthy is that the Fe substitution for Co in $Sr_3(Co_{0.9-x}Fe_xNb_{0.1})_2O_{7-\delta}$ ($0 \leq x \leq 1$) yields a volcano-like activity trend with 10% Fe substitution (ie, RP-SCFN) being the most active composition (Figures 2F and S8). Thus, a low level of Fe doping contributes to the further activity enhancement, which has been widely reported in previous studies due

to favorable electronic modifications.[31,35-37] Figure 2G compares the OER activity (ie, η@10 mA cm_{geo}^{-2}, one practical parameter to assess water-splitting devices[32,38]) of RP-SCFN with present state-of-the-art oxide-based catalysts on GC in 0.1 M KOH solution, including spinel oxides, Li-based oxides, simple perovskites, double perovskites, complex oxides, and hybrid oxides (Table S2). As shown, the OER activity of RP-SCFN ranks among the highest oxide-based catalysts in alkaline media ever reported. Besides the activity, the RP-SCFN shows much better durability than the benchmark RuO_2 catalyst (Figure S9), demonstrating its value for practical application. The poor stability of RuO_2 is due to the oxidation of surface Ru^{4+} to soluble RuO_4^{2-} anions under OER conditions.[39]

2.3 | Electronic structure characterization

To identify the origin of the high OER activity of RP-SCFN, we resort to the advanced surface-sensitive sXAS measured with total electron yield (TEY) mode to investigate the electronic structures. sXAS in TEY mode is a well-known technique to glean the information of surface electronic structures and has a typical probing depth of ~5 nm.[40-43] Figure 3A shows the Co L_3-edge sXAS spectra of RP-SCFN and P-SCFN, as well as the reference materials with different valence states including divalent CoO, trivalent $EuCoO_3$,[44] and tetravalent $SrCoO_3$.[45] The Co L-edge XAS is highly sensitive to the Co valence states. The Co L_3-edge peak shifts to higher energy from CoO to $EuCoO_3$, P-SCFN, RP-SCFN, and further $SrCoO_3$, reflecting the coexistence of Co^{3+}/Co^{4+} in RP-SCFN as well as higher Co valence state of RP-SCFN relative to P-SCFN. By comparing the Co L_3-edge peak position with reference samples, the average Co valence state of RP-SCFN was calculated to be ~ + 3.44, close to the optimal value of +3.4 in highly active $SrCoO_{2.7}$ catalyst.[14] To note, a small peak at 777.8 eV of CoO spectrum as a fingerprint of Co^{2+} was present for P-SCFN (but absent for RP-SCFN), indicating that some Co^{2+} ions are in P-SCFN and excluded for RP-SCFN. Besides, the XAS spectra of Fe-L_3 and Nb-L_3 depicted in Figure 3B,C display nearly the same between RP-SCFN and P-SCFN, implying no distinct change in the surface Fe and Nb oxidation state for RP-SCFN and P-SCFN. It is well known that for the later 3d transition metal oxides, the ground state can be described by $\Phi = \alpha d^n > +\beta d^{n+1}\underline{L} > +\gamma d^{n+2}\underline{L}^2 >$ and the charge transfer energy (Δ) decrease by about 4 eV if the Co valence increases by one in the charge transfer

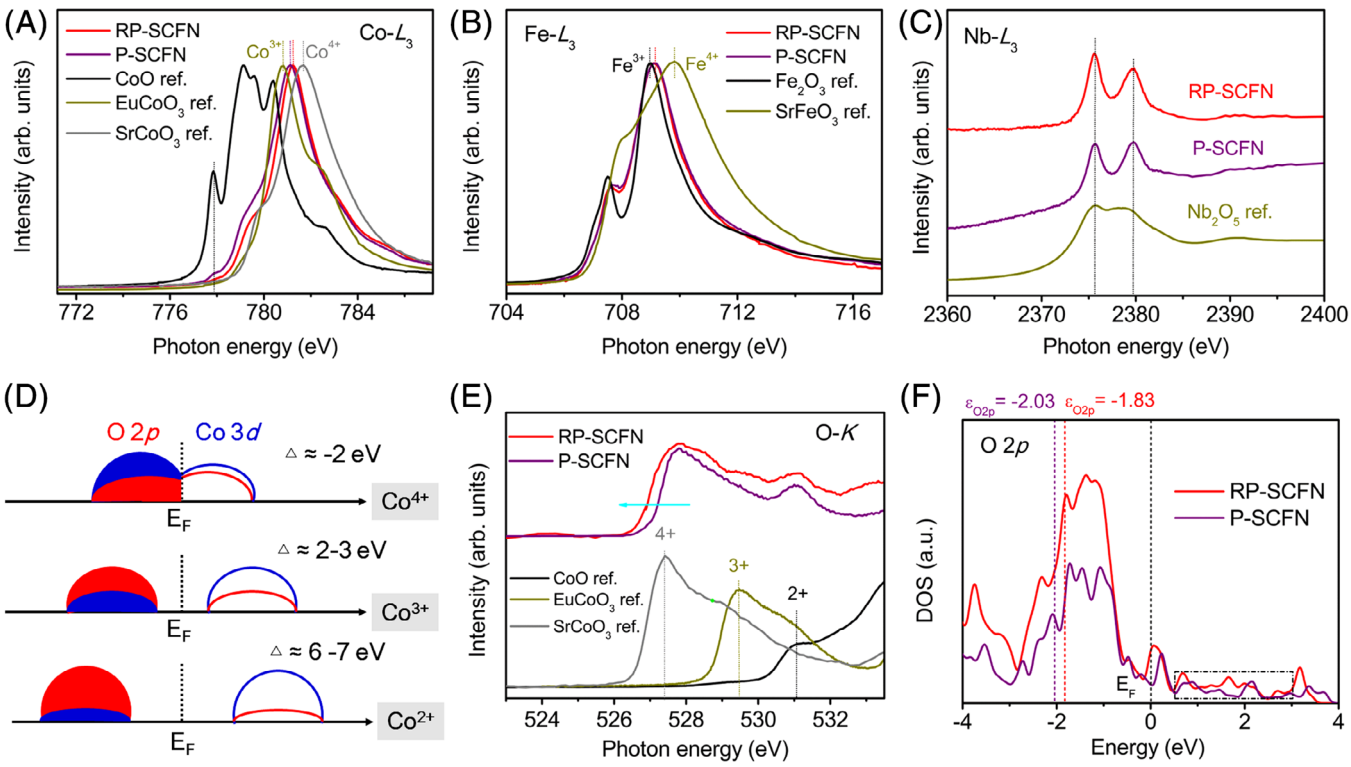

FIGURE 3 The, A, Co-L_3, B, Fe-L_3, and, C, Nb-L_3 sXAS spectra of RP-SCFN, P-SCFN, and several reference materials. D, Charge-transfer models of Co^{2+}, Co^{3+}, and Co^{4+} in covalent systems. E, The O-K sXAS spectra of RP-SCFN, P-SCFN, and several reference materials. F, Projected density of states of O 2p and calculated O 2p-band center on RP-SCFN and P-SCFN. P-SCFN, $SrCo_{0.8}Fe_{0.1}Nb_{0.1}O_{3-\delta}$ perovskite; RP-SCFN, Ruddlesden-Popper $Sr_3(Co_{0.8}Fe_{0.1}Nb_{0.1})_2O_{7-\delta}$

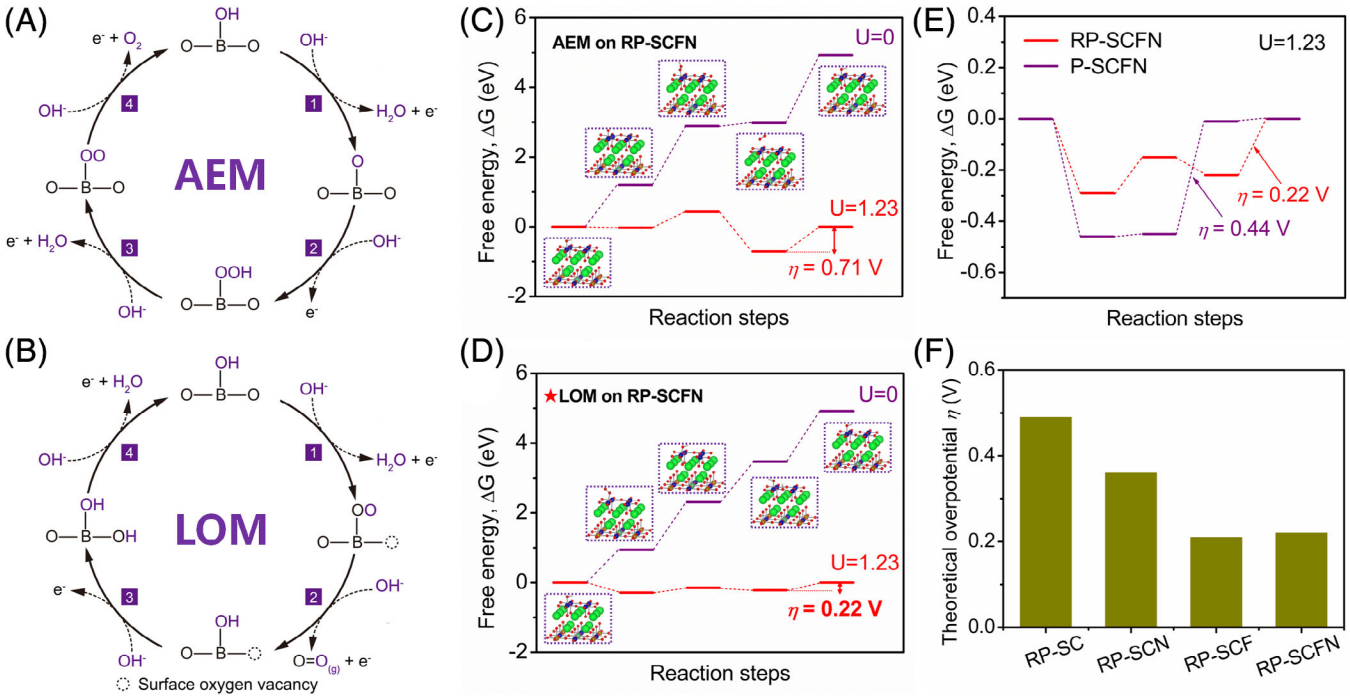

FIGURE 4 A, AEM. B, LOM. Free energies of OER steps under potential $U = 0$ and 1.23 V via, C, AEM and, D, LOM on RP-SCFN. E, Free energies of OER steps under potential 1.23 V via LOM on RP-SCFN and P-SCFN. F, Theoretical overpotential η of RP-SC, RP-SCN, RP-SCF, and RP-SCFN. AEM, adsorbate evolution mechanism; LOM, lattice-oxygen oxidation mechanism; OER, oxygen evolution reaction; P-SCFN, $SrCo_{0.8}Fe_{0.1}Nb_{0.1}O_{3-\delta}$ perovskite; RP-SCFN, Ruddlesden-Popper $Sr_3(Co_{0.8}Fe_{0.1}Nb_{0.1})_2O_{7-\delta}$

models as shown in Figure 3D.[42,46-48] In this case, Δ reduces from a large positive value of 6 to 7 eV for Co^{2+} with a dominant $3d^n$ configuration to a negative value for Co^{4+} with a dominant $3d^{n+1}\underline{L}$ configuration. Here, $\underline{L}$ denotes ligand oxygen 2*p* hole which is originated from strong oxygen 2*p* and cobalt 3*d* covalence. This means that the lattice-oxygen oxidation for Co^{4+} oxides is due to its great covalency of metal-oxygen bonds.[13,17,43,48] Thus, high content of Co^{4+} renders RP-SCFN as a highly covalent oxide. The O *K*-edge sXAS spectra were further collected to explore the covalency between O 2*p* and transition metal 3*d* states.[42,43,49,50] It is known that the pre-edge peaks below ~532 eV in the O-*K* XAS spectra represent the unoccupied O 2*p* orbitals hybridized with transition metal 3*d* orbitals.[42,43,49,50] Figure 3E (bottom) shows that the O-*K* pre-edge peak shifts to lower energies and the spectral weight increases as the Co valence increases from Co^{2+} to Co^{3+} and further to Co^{4+}, suggesting an increased degree of covalency between Co 3*d* and O 2*p* states. Lower O-*K* pre-edge energy position and higher level of spectral weight were observed for RP-SCFN relative to P-SCFN, demonstrating the enhanced metal-oxygen covalency for the former as further conformed by the calculated density of states of O 2*p*. The O 2*p*-band center was also calculated considering that it has been reported to correlate with the covalence and OER activity.[17,31,51,52] As seen from Figure 3F, the O 2*p*-band center (−1.83 eV) of RP-SCFN is closer to the Fermi level than that (−2.03 eV) of P-SCFN, implying that RP-SCFN would boost the OER. According to the above analysis, we can conclude that strong metal-oxygen covalency can be induced by the engineered RP phase, which is critical to trigger lattice-oxygen oxidation.

2.4 | Density functional theory calculations

Density functional theory calculations were further performed to understand the reaction mechanism and possible active sites of RP-SCFN. Two different OER mechanisms, that is, adsorbate evolution mechanism (AEM) and LOM were considered (Figure 4A,B). The conventional AEM concerning cation redox proceeds through four concerted proton-electron transfer steps with multiple adsorbed intermediates, resulting in a minimum theoretical overpotential of ~ 0.37 V.[1,53,54] The recently accepted LOM involves a lattice-oxygen oxidation and nonconcerted proton-electron transfer, which can bypass the limitation for AEM and potentially offer better OER activity.[15,17,54] Figure 4C,D shows the free energy diagrams under potential U = 0 and 1.23 V of RP-SCFN via AEM and LOM. As can be seen, the theoretical thermodynamic overpotential (η) of RP-SCFN based on LOM was calculated to be 0.22 V, significantly lower than the value (0.71 V) via AEM, implying that the

lattice oxygen in RP-SCFN is OER active sites. Such a theoretical η (0.22 V) for RP-SCFN is even lower than the reported state-of-the-art oxides with activated oxygen sites, such as $Zn_{0.2}Co_{0.8}OOH$ (0.27 V)[54] and $La_{0.5}Ba_{0.25}Sr_{0.25}CoO_{2.9-\delta}F_{0.1}$ (0.27 V).[55] The high activity of lattice oxygen in RP-SCFN could be ascribed to its strong metal-oxygen covalency, as demonstrated by aforementioned XAS analysis. As compared with the P-SCFN, the RP-SCFN also gives rise to lower η value (Figure 4E). In order to explore the role of composed elements (eg, Nb and Fe) on the activity of RP-SCFN, the free energies of Nb/Fe-free RP-SC, Fe-free RP-SCN and Nb-free RP-SCF based on AEM and LOM were also calculated (Figure S10). All RP-structured oxides generate much lower η values via LOM than AEM, addressing the dominating role of RP structure on activating lattice oxygen. Fe- containing RP-SCF and RP-SCFN samples show lower theoretical LOM η than Fe-free RP-SC and RP-SCN, respectively, which indicates that a low level of Fe doping in RP-SCFN can further enhance the activity (Figure 4F). Slight Nb^{5+} content in RP-SCFN is just to help stabilize the crystal structure, evidenced by the unsuccessful pure phase formation in Nb-free RP-SC and RP-SCF. This is also supported well by the fact that RP-SCF and RP-SCFN possess nearly the same theoretical LOM η. Overall, the above theoretical calculations demonstrate the lattice oxygen ions in RP-SCFN as active sites for OER and critical role of low-level Nb/Fe co-doping, which cooperatively contributes to the outstanding OER activity of RP-SCFN.

3 | CONCLUSION

In summary, we have demonstrated for the first time that the lattice-oxygen in RP oxides can be activated for boosting OER. As a model catalyst, the bulk $Sr_3(Co_{0.8}Fe_{0.1}Nb_{0.1})_2O_{7-\delta}$ (RP-SCFN) synthesized by the facile and scalable sol-gel method shows ultrafast OER activity (including MA and SA), which is much higher than the simple P-SCFN and benchmark RuO_2 catalyst. Remarkably, the RP-SCFN achieves an extremely low overpotential of 334 mV at 10 mA cm^{-2} and a small Tafel slope of 57 mV dec^{-1} in 0.1 M KOH solution, surpassing most state-of-the-art oxide-based catalysts ever reported. The LOM was demonstrated to be proceeded on RP-SCFN by first-principle calculations, arising from its strong metal-oxygen covalency with favorable electronic structure. This work opens new avenues for developing highly active electrocatalysts for OER and other heterogeneous catalysis by unique structural design and lattice oxygen redox processes.

ACKNOWLEDGMENTS

This work was financially supported by the Australian Research Council (Discovery Early Career Researcher Award No. DE190100005). Computational work was supported by resources provided by the Pawsey Supercomputing Centre with funding from the Australian National Computational and the Government of Western Australia. We acknowledge support from the Max Planck-POSTECH-Hsinchu Center for Complex Phase Materials and the staff of Monash Center for Electron Microscopy.

ORCID

Yinlong Zhu https://orcid.org/0000-0002-9207-2452

REFERENCES

1. Seh ZW, Kibsgaard J, Dickens CF, Chorkendorff L, Nørskov JK, Jaramillo TF. Combining theory and experiment in electrocatalysis: insights into materials design. *Science*. 2017; 355:eaad4998.
2. Katsounaros I, Cherevko S, Zeradjanin AR, Mayrhofer KJ. Oxygen electrochemistry as a cornerstone for sustainable energy conversion. *Angew Chem Int Ed*. 2014;53:102-121.
3. Song F, Bai L, Moysiadou A, et al. Transition metal oxides as electrocatalysts for the oxygen evolution reaction in alkaline solutions: an application-inspired renaissance. *J Am Chem Soc*. 2018;140:7748-7759.
4. Hwang J, Rao RR, Giordano L, Katayama Y, Yu Y, Shao-Horn Y. Perovskites in catalysis and electrocatalysis. *Science*. 2017;358:751-756.
5. Seitz LC, Dickens CF, Nishio K, et al. A highly active and stable $IrO_x/SrIrO_3$ catalyst for the oxygen evolution reaction. *Science*. 2016;353:1011-1014.
6. Dai J, Zhu Y, Yin Y, et al. Super-exchange interaction induced overall optimization in ferromagnetic perovskite oxides enables ultrafast water oxidation. *Small*. 2019;15:1903120.
7. She S, Zhu Y, Chen Y, Lu Q, Zhou W, Shao Z. Realizing ultrafast oxygen evolution by introducing proton acceptor into perovskites. *Adv Energy Mater*. 2019;9:1900429.
8. Suntivich J, May KJ, Gasteiger HA, Goodenough JB, Shao-Horn Y. A perovskite oxide optimized for oxygen evolution catalysis from molecular orbital principles. *Science*. 2011;334: 1383-1385.
9. Calle-Vallejo F, Inoglu NG, Su HY, et al. Number of outer electrons as descriptor for adsorption processes on transition metals and their oxides. *Chem Sci*. 2013;4:1245-1249.
10. Lim T, Niemantsverdriet JW, Gracia J. Layered antiferromagnetic ordering in the most active perovskite catalysts for the oxygen evolution reaction. *ChemCatChem*. 2016;8:2968-2974.
11. Zhu Y, Zhou W, Chen Z, et al. $SrNb_{0.1}Co_{0.7}Fe_{0.2}O_{3-\delta}$ perovskite as a next-generation electrocatalyst for oxygen evolution in alkaline solution. *Angew Chem Int Ed*. 2015;54:3897-3901.
12. Grimaud A, Hong WT, Shao-Horn Y, Tarascon JM. Anionic redox processes for electrochemical devices. *Nat Mater*. 2016; 15:121-126.
13. Grimaud A, Demortière A, Saubanère M, et al. Activation of surface oxygen sites on an iridium-based model catalyst for the oxygen evolution reaction. *Nat Energy*. 2017;2:16189.
14. Tyler MJ, Rong X, Abakumov AM, et al. Water electrolysis on $La_{1-x}Sr_xCoO_{3-\delta}$ perovskite electrocatalysts. *Nat Commun*. 2016; 7:11053.
15. Yoo JS, Rong X, Liu Y, Kolpak AM. Role of lattice oxygen participation in understanding trends in the oxygen evolution reaction on perovskites. *ACS Catal*. 2018;8:4628-4636.

16. Yang C, Grimaud A. Factors controlling the redox activity of oxygen in perovskites: from theory to application for catalytic reactions. *Catalysts*. 2017;7:149.
17. Grimaud A, Diaz-Morales O, Han B, et al. Activating lattice oxygen redox reactions in metal oxides to catalyse oxygen evolution. *Nat Chem*. 2017;9:457-465.
18. Yagi S, Yamada I, Tsukasaki H, et al. Covalency-reinforced oxygen evolution reaction catalyst. *Nat Commun*. 2015;6:8249.
19. Kim NI, Sa YJ, Yoo TS, et al. Oxygen-deficient triple perovskites as highly active and durable bifunctional electrocatalysts for oxygen electrode reactions. *Sci Adv*. 2018;4:eaap9360.
20. Yamada I, Fujii H, Takamatsu A, et al. Bifunctional oxygen reaction catalysis of quadruple manganese perovskites. *Adv Mater*. 2017;29:1603004.
21. Kim J, Shih PC, Qin Y, Al-Bardan Z, Sun CJ, Yang H. A porous pyrochlore $Y_2[Ru_{1.6}Y_{0.4}]O_{7-\delta}$ electrocatalyst for enhanced performance towards the oxygen evolution reaction in acidic media. *Angew Chem Int Ed*. 2018;130:14073-14077.
22. Zhu Y, Zhou W, Chen Y, Shao Z. An Aurivillius oxide based cathode with excellent CO_2 tolerance for intermediate-temperature solid oxide fuel cells. *Angew Chem Int Ed*. 2016;55:8988-8993.
23. Zhu Y, Tahini HA, Hu Z, et al. Unusual synergistic effect in layered Ruddlesden-Popper oxide enables ultrafast hydrogen evolution. *Nat Commun*. 2019;10:149.
24. Forslund RP, Hardin WG, Rong X, et al. Exceptional electrocatalytic oxygen evolution via tunable charge transfer interactions in $La_{0.5}Sr_{1.5}Ni_{1-x}Fe_xO_{4\pm\delta}$ Ruddlesden-Popper oxides. *Nat Commun*. 2018;9:3150.
25. Jumi B, Bae HB, Kim J, Oh J, Chung SY. Formation of two-dimensional homologous faults and oxygen electrocatalytic activities in a perovskite nickelate. *Nano Lett*. 2017;17:3126-3132.
26. Abrishami ME, Risch M, Scholz J, Roddatis V, Osterthun N, Jooss C. Oxygen evolution at manganite perovskite Ruddlesden-Popper type particles: trends of activity on structure, valence and covalence. *Materials*. 2016;9:921.
27. Nakamura T, Ling Y, Amezawa K. The effect of interstitial oxygen formation on the crystal lattice deformation in layered perovskite oxides for electrochemical devices. *J Mater Chem A*. 2015;3:10471-10479.
28. Nagai T, Ito W, Sakon T. Relationship between cation substitution and stability of perovskite structure in $SrCoO_{3-\delta}$-based mixed conductors. *Solid State Ion*. 2007;177:3433-3444.
29. Zhou W, Shao Z, Ran R, Jin W, Xu N. A novel efficient oxide electrode for electrocatalytic oxygen reduction at 400-600 °C. *Chem Commun*. 2008;44:5791-5793.
30. Suntivich J, Gasteiger HA, Yabuuchi N, Shao-Horn Y. Electrocatalytic measurement methodology of oxide catalysts using a thin-film rotating disk electrode. *J Electrochem Soc*. 2010;157:B1263-B1268.
31. Wu T, Sun S, Song J, et al. Iron-facilitated dynamic active-site generation on spinel $CoAl_2O_4$ with self-termination of surface reconstruction for water oxidation. *Nat Catal*. 2019;2:763-772.
32. McCrory CC, Jung S, Peters JC, Jaramillo TF. Benchmarking heterogeneous electrocatalysts for the oxygen evolution reaction. *J Am Chem Soc*. 2013;135:16977-16987.
33. Chao W, Rao RR, Peng J, et al. Recommended practices and benchmark activity for hydrogen and oxygen electrocatalysis in water splitting and fuel cells. *Adv Mater*. 2019;2:1806296.
34. Giordano L, Han B, Risch M, et al. pH dependence of OER activity of oxides: current and future perspectives. *Catal Today*. 2016;262:2-10.
35. Zhu Y, Zhou W, Chen Y, Yu J, Liu M, Shao Z. A high-performance electrocatalyst for oxygen evolution reaction: $LiCo_{0.8}Fe_{0.2}O_2$. *Adv. Mater*. 2015;27:7150-7155.
36. Zhou Y, Sun S, Song J, et al. Enlarged Co-O covalency in octahedral sites leading to highly efficient spinel oxides for oxygen evolution reaction. *Adv Mater*. 2018;30:1802912.
37. Kim BJ, Fabbri E, Abbott DF, et al. Functional role of Fe-doping in Co-based perovskite oxide catalysts for oxygen evolution reaction. *J Am Chem Soc*. 2019;141:5231-5240.
38. Chao W, Xu ZJ. The comprehensive understanding of as an evaluation parameter for electrochemical water splitting. *Small Methods*. 2018;2:1800168.
39. Zhu Y, Tahini HA, Wang Y, et al. Pyrite-type ruthenium disulfide with tunable disorder and defects enables ultra-efficient overall water splitting. *J Mater Chem A*. 2019;7:14222-14232.
40. Zhang B, Zheng X, Voznyy O, et al. Homogeneously dispersed multimetal oxygen-evolving catalysts. *Science*. 2016;352:333-337.
41. Feng L, Markus IM, Nordlund D, et al. Surface reconstruction and chemical evolution of stoichiometric layered cathode materials for lithium-ion batteries. *Nat Commun*. 2014;5:3529.
42. Reiko N, Stöhr J, Idzerda YU. Electron-yield saturation effects in L-edge x-ray magnetic circular dichroism spectra of Fe, Co, and Ni. *Phys Rev B*. 1999;59:6421.
43. Zhu Y, Tahini HA, Hu Z, et al. Boosting oxygen evolution reaction by creating both metal ion and lattice-oxygen active sites in a complex oxide. *Adv Mater*. 2020;32:1905025.
44. Hu Z, Wu H, Haverkort MW, et al. Different look at the spin state of ions in a pyramidal coordination. *Phys Rev Lett*. 2004;92:207402.
45. Potze RH, Sawatzky GA, Abbate M. Possibility for an intermediate-spin ground state in the charge-transfer material $SrCoO_3$. *Phys Rev B*. 1995;51:11501-11506.
46. Fujimori A, Bocquet AE, Saitoh T, Mizokawa T. Electronic structure of 3d transition metal compounds: systematic chemical trends and multiplet effects. *J Electron Spectrosc Relat Phenom*. 1993;62:141-152.
47. van der Laan G, Zaanen J, Sawatzky GA, Karnatak R, Esteva JM. Comparison of X-ray absorption with X-ray photoemission of nickel dihalides and NiO. *Phys Rev B*. 1986;33:4253-4263.
48. Hong WT, Stoerzinger KA, Lee YL, et al. Charge-transfer-energy-dependent oxygen evolution reaction mechanisms for perovskite oxides. *Energ Environ Sci*. 2017;10:2190-2200.
49. Mizokawa T, Wakisaka Y, Sudayama T, et al. Role of oxygen holes in Li_xCoO_2 revealed by soft X-Ray spectroscopy. *Phys Rev Lett*. 2013;111:056404.
50. Wang X, Pan Z, Chu X, et al. Atomic-scale insights into surface lattice oxygen activation at the spinel/perovskite interface of $Co_3O_4/La_{0.3}Sr_{0.7}CoO_3$. *Angew Chem Int Ed*. 2019;131:11846-11851.

51. Grimaud A, May KJ, Carlton CE, et al. Double perovskites as a family of highly active catalysts for oxygen evolution in alkaline solution. *Nat Commun*. 2013;4:2439.
52. Ryan J, Hwang J, Shao-Horn Y, Morgan D. Assessing correlations of perovskite catalytic performance with electronic structure descriptors. *Chem Mater*. 2019;31:785-797.
53. Man IC, Su HY, Calle-Vallejo F, et al. Universality in oxygen evolution electrocatalysis on oxide surfaces. *ChemCatChem*. 2011;3:1159-1165.
54. Huang Z, Song J, Du Y, et al. Chemical and structural origin of lattice oxygen oxidation in Co-Zn oxyhydroxide oxygen evolution electrocatalysts. *Nat Energy*. 2019;4:329-338.
55. Hua B, Li M, Pang W, et al. Activating p-blocking centers in perovskite for efficient water splitting. *Chem*. 2018;4:2902-2916.

SUPPORTING INFORMATION

Additional supporting information may be found online in the Supporting Information section at the end of this article.

How to cite this article: Zhu Y, Tahini HA, Hu Z, et al. Boosting oxygen evolution reaction by activation of lattice-oxygen sites in layered Ruddlesden-Popper oxide. *EcoMat*. 2020;2:e12021. https://doi.org/10.1002/eom2.12021